Transient Stability Evaluation and Decoupled Control for Grid-Following Converters Considering Nonideal Alternating Current Control

Xilin Li, Pan Feng, Ruiqi Zhang, Zhen Tian, *Member, IEEE*, Meng Huang, *Member, IEEE*, Xiaoming Zha, *Senior Member, IEEE*, Xiaoling Xiong, *Member, IEEE*, and Pan Hu, *Senior Member, IEEE*

***Abstract*—In most previous studies about transient synchronization stabilities of grid-following converters (GFLC), alternating current control (ACC) dynamics are often neglected. However, the bandwidth of the ACC cannot be selected too high in some low-switching cases, such as large wind turbines. The adverse effects of ACC must be considered to avoid over-optimistic evaluation of transient stability. There are seldom quantitative and analytic large signal analyses that take the ACC dynamics into account. To fill this gap, an iteration-based accurate transient stability evaluation method is proposed in this article. First, the model of the ACC and line dynamics are deduced. The time-domain analytic solution of current dynamics is obtained. Furthermore, the multivariate implicit function equation set concerning current-frequency-power angle's mapping relation under the critical stable condition is constructed and the transient stability boundary is solved based on the proposed iterative algorithm. The interaction mechanism between the phase-locked-loop (PLL) and ACC is accurately quantified. A simplified transient stability criterion is deduced to preliminarily estimate the adverse effects of ACC on GFLC's transient stability. In addition, a stability-enhanced decoupled PLL strategy is proposed to enable the setting of PLL bandwidth unconstrained by the interaction from ACC, which significantly improves the dynamic response of the GFLC. Simulation and experiments verify the effectiveness and superiority of the proposed stability evaluation method and decoupled PLL strategy.**

***Index Terms*—Alternating current control (ACC), equal area criterion (EAC), grid-following converter (GFLC), iterative algorithm, phase-locked-loop (PLL), transient synchronization stability.**

Received 15 October 2024; revised 10 January 2025; accepted 29 January 2025. Date of publication 4 February 2025; date of current version 14 April 2025. This work was supported by the Science and Technology Project of State Grid Corporation of China under Project 4000-202399378A-2-2-ZB. Recommended for publication by Associate Editor A. Kuperman. *(Corresponding authors: Zhen Tian; Xiaoming Zha.)*

Xilin Li, Pan Feng, Ruiqi Zhang, Zhen Tian, Meng Huang, and Xiaoming Zha are with the Hubei Key Laboratory of Power Equipment & System Security for Integrated Energy, School of Electrical Engineering and Automation, Wuhan University, Wuhan 430072, China (e-mail: snplee@whu.edu.cn; 2023202070069@whu.edu.cn; 2021302191486@whu.edu.cn; ztian.ee@whu.edu.cn; meng.huang@whu.edu.cn; xmzha@whu.edu.cn).

Xiaoling Xiong is with the School of Electrical & Electronic Engineering, North China Electric Power University, Beijing 102206, China (e-mail: xiongxl1102@ncepu.edu.cn).

Pan Hu is with the State Grid Hubei Electric Power Research Institute, Wuhan 430048, China (e-mail: hupaninwh@whu.edu.cn).

Color versions of one or more figures in this article are available at https://doi.org/10.1109/TPEL.2025.3538523.

Digital Object Identifier 10.1109/TPEL.2025.3538523

I. Introduction

THE transient synchronization stability of grid-following converters (GFLC) has been widely evaluated and is assumed to be dominated by the dynamics of phase-locked-loops (PLLs) [1], [2], [3], [4], [5]. The inner alternating current control (ACC) is usually assumed under a quasi-steady state due to its high bandwidth. Therefore, the ACC dynamics are usually neglected to reduce model order and simplify the difficulties in transient stability analysis. However, the ACC bandwidth setting is constrained by the converter switching frequency. The bandwidth of ACC cannot be selected too high in low-switching cases, such as high-power converters for large wind turbines [6]. Consequently, the dynamics of ACC must be captured when analyzing GFLC's transient stability. Plenty of studies have analyzed the interaction between PLL and ACC based on small signal-based methods [7], [8], [9], [10]. But they are invalid under large disturbance. Only seldom studies analyzed the transient stability of GFLC considering ACC's impact.

The transient coupling between the nonideal ACC and PLL is found in [11]. Simulation results reveal that ignorance of ACC yields over-optimistic transient stability assessment. A synchronous generator-analogized model of the GFLC is developed in [12]. The mechanism by which ACC deteriorates stability is revealed as the acceleration of PLL's equivalent motion, but the amount of accelerating area increased by ACC is not quantified. A Lyapunov function that considers ACC's coupling effects is constructed in [13] to reveal the instability mechanism caused by ACC's interaction. Equal area criterion (EAC) is applied in [6] to evaluate GFLC's transient synchronization stability and a bandwidth boundary whether the current dynamics can be ignored is proposed. However, the impacts of ACC's coupling cannot be analytically quantified in both [6] and [13], and can only be obtained by time-domain numerical calculation. Takagi-Sugeno method is applied in [14] to capture ACC's impacts in stable domain derivation, but cannot reveal parameters' impact mechanisms. A numerical continuation method is proposed based on bifurcation theory in [15] to capture ACC's transient effects on PLL. Both [14] and [15] are facing the challenge of intensive computation burden and are not applicable for online stability evaluation. A step-to-step model reduction analysis is conducted in [16]. It is found that ignorance of filter capacitors will not yield much error, but the dynamics of ACC and grid inductors

cannot be ignored. Furthermore, a simplified transient model is established in [17], which can capture the dominant dynamics of ACC. However, the analyses in [16] and [17] are based on the simulation results, which lack mechanism revelation. To simplify the coupling between PLL and ACC, a slow–fast subsystem is established in [18], based on the singular perturbation method. However, Lyapunov-based stability analyses are conducted on the slow and fast subsystems separately, and how the two subsystems' interaction affects each other's transient stability remains unknown. Li et al. [19] proposed an inequality scaling-combined EAC method that analytically assesses ACC's worst impacts on GFLC's transient stability but with considerable conservatism. Xu et al. [20] analyze the transient stability of GFLC considering ACC impacts and conducts parameters design, with the aid of phase portrait. However, the phase portrait method is similar to the simulation-based method and the conclusions drawn are only verified in specific conditions.

Striping of PLL dynamics from ACC dynamics can be achieved by feedforwarding PLL output frequency. This can help partially reduce ACC's detrimental effects on PLL transient synchronization stability. To fully reveal how the ACC affects system's transient stability, an iteration-based EAC is proposed in this article, which is partially based on the iterative EAC in our earlier paper [5]. A multivariate implicit function equation set (IFES) concerning current-frequency-power angle's mapping relation under the critical stable condition is constructed and the transient stability boundary is thus iteratively solved. Due to the full consideration of both ACC dynamics and damping effects, the conservatism of the proposed stability evaluation method is relatively low. Furthermore, a simplified criterion is proposed to quickly assess ACC's impacts on GFLC's transient stability. Moreover, a stability-enhanced decoupled PLL strategy is proposed to make the parameters setting of PLL unconstrained by the interaction from ACC.

The rest of this article is organized as follows. Section II derives the 6th-order nonlinear model of GFLC, which fully considers ACC, PLL, and grid line dynamics. The transient stability boundary that captures ACC's impacts is iteratively obtained in Section III. Another simplified criterion is also introduced in Section III, with less computation but more conservatism. Parameters impact analysis, method comparison, and a stability-enhanced decoupled PLL strategy are given in Section IV. Simulation and experiment verification are conducted in Sections V and VI, respectively. Finally, Section VII concludes this article.

II. Sixth-Order Model Derivation

The analyzed GFLC system is shown in Fig. 1. V_g and θ_g are the grid voltage's amplitude and phase, respectively. L_g and R_g are the inductance and resistance of the grid line, respectively. L_f denotes the output filter of the GFLC. The converter's controller contains a PLL and an ACC. The dc-link voltage variation is ignored during the transient process due to the chopper circuit. K_P and K_I denote the PLL's proportional-integral (PI) parameters. K_{CP} and K_{CI} are the PI parameters of ACC. PLL outputs the reference phase θ_{PLL} and frequency ω_{PLL} by input point

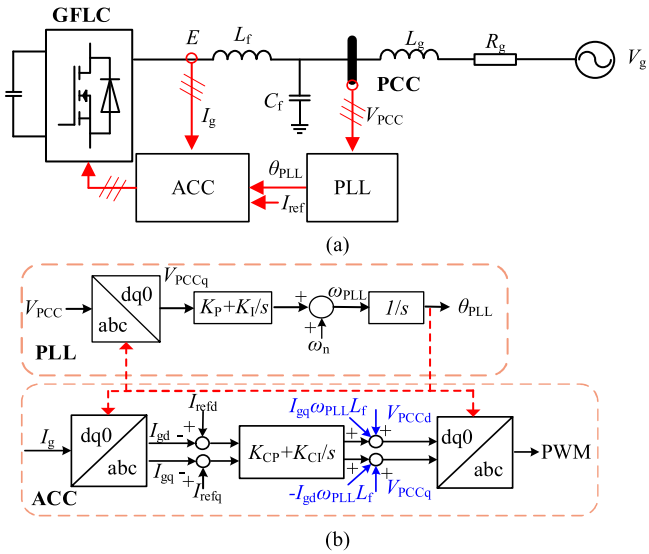

Fig. 1. Structure of the analyzed GFLC connected to the grid system. (a) The simplified diagram of circuit structure. (b) The diagram of controller structure.

of common coupling (PCC) voltage V_{PCC}. ω_{n} is the frequency nominal value. The ACC regulates the output current based on the dq-axis reference current I_{refd}, I_{refq}, and reference phase θ_{PLL}. Neglecting variation of grid frequency ω_g, it can be assumed that $\omega_g = \omega_n$. I_{gd} and I_{gq} are the dq-axis components of line current, respectively. It is mentioned that all the Park transformations in this article are conducted with θ_{PLL} as the reference phase.

A. Modeling of the ACC and Line Current Dynamic

According to the Kirchhoff's voltage law, the dq-axis components of V_{PCC} can be derived as

$$\begin{aligned} V_{\mathrm{PCC}d} &= V_g \cos\delta - \omega_{\mathrm{PLL}} L_g I_{gq} + R_g I_{gd} + L_g \mathrm{d}I_{gd}/\mathrm{d}t \\ V_{\mathrm{PCC}q} &= -V_g \sin\delta + \omega_{\mathrm{PLL}} L_g I_{gd} + R_g I_{gq} + L_g \mathrm{d}I_{gq}/\mathrm{d}t. \end{aligned} \quad (1)$$

E_d and E_q are the output voltage of GFLC and can be derived also based on Kirchhoff's voltage law

$$\begin{aligned} E_d &= V_g \cos\delta + R_g I_{gd} - \omega_{\mathrm{PLL}} (L_g + L_f) I_{gq} \\ &\quad + (L_g + L_f) \frac{\mathrm{d}I_{gd}}{\mathrm{d}t} \\ E_q &= -V_g \sin\delta + R_g I_{gq} + \omega_{\mathrm{PLL}} (L_g + L_f) I_{gd} \\ &\quad + (L_g + L_f) \frac{\mathrm{d}I_{gq}}{\mathrm{d}t}. \end{aligned} \quad (2)$$

Considering the high switching frequency of PWM, E_{dq} can be assumed to equal the output of ACC, which can be derived according to the ACC controller structure in Fig. 1

$$\begin{aligned} E_d &= V_{\mathrm{PCC}d} + k_{\mathrm{CI}} \int (I_{\mathrm{refd}} - I_{gd})\mathrm{d}t + k_{\mathrm{CP}}(I_{\mathrm{refd}} - I_{gd}) \\ &\quad - \omega_{\mathrm{PLL}} L_f I_{gq} \\ E_q &= V_{\mathrm{PCC}q} + k_{\mathrm{CI}} \int (I_{\mathrm{refq}} - I_{gq})\mathrm{d}t + k_{\mathrm{CP}}(I_{\mathrm{refq}} - I_{gq}) \end{aligned}$$

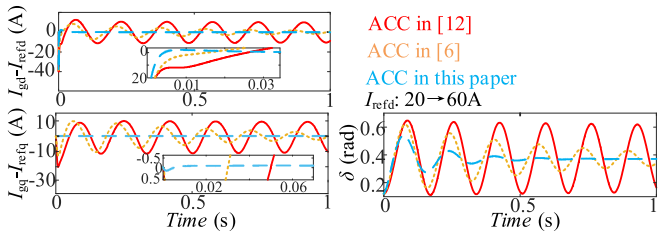

Fig. 2. Comparison of different ACCs under large disturbance.

$$+\omega_{\text{PLL}} L_f I_{gd}. \tag{3}$$

Combing (1)–(3), the dynamics of ACC are deduced as

$$\begin{aligned} L_f \mathrm{d}I_{gd}/\mathrm{d}t &= +k_{\text{CI}} \int (I_{\text{ref}d} - I_{gd})\mathrm{d}t + k_{\text{CP}} (I_{\text{ref}d} - I_{gd}) \\ L_f \mathrm{d}I_{gq}/\mathrm{d}t &= +k_{\text{CI}} \int (I_{\text{ref}q} - I_{gq})\mathrm{d}t + k_{\text{CP}} (I_{\text{ref}q} - I_{gq}) . \end{aligned} \tag{4}$$

It is seen that with the help of the feed-forward terms: $\omega_{\text{PLL}} L_f I_{\text{ref}q} + V_{\text{PCC}d}$ and -$\omega_{\text{PLL}} L_f I_{\text{ref}d} + V_{\text{PCC}q}$, the PLL dynamic and grid voltage values are peeled off in the ACC dynamic. This also means that the different ACCs in multi-GFLC paralleled systems do not interact with each other. Wu et al. [6] and Hu et al. [12] point out that grid-side coupling is the dominant factor leading to ACC transient dynamics, which further yields significant adverse impacts on PLL's transient stability. However, this conclusion is mainly attributed to the ACC without appropriate feed-forward terms. As shown in Fig. 2, the ACC with approximate feed-forward terms adopted in this article exhibits faster response speed, while the ACCs with insufficient feed-forward terms [6], [12] are influenced by the slow dynamics of PLL. In addition, the *dq*-axis currents are also decoupled from each other, according to (4). System (4) can be decoupled into two 2nd-order linear time-invariant systems and their analytical time-domain solution can be simply solved based on the linear system theory

$$\begin{aligned} I_{gd}(t) &= I_{\text{ref}d+} - A_1 e^{m_1 t} - A_2 e^{m_2 t} \\ I_{\text{gq}}(t) &= I_{\text{ref}q+} - A_3 e^{m_1 t} - A_4 e^{m_2 t} \\ \dot{I}_{gd}(t) &= -A_1 m_1 e^{m_1 t} - A_2 m_2 e^{m_2 t} \\ \dot{I}_{gq}(t) &= -A_3 m_1 e^{m_1 t} - A_4 m_2 e^{m_2 t}. \end{aligned} \tag{5}$$

The current expression in (5) is based on the premise that the ACC is overdamped, i.e., $K^2_{\text{CP}} > 4K_{\text{CI}}L_f$, which is always true in practice to avoid unexpected oscillation. The constant coefficients m_1–m_2 and A_1–A_4 in (5) are denoted as

$$\begin{aligned} A_1 &= m_1 \frac{I_{\text{ref}d+} - I_{\text{ref}d-}}{m_1 - m_2} \\ A_2 &= m_2 \frac{I_{\text{ref}d+} - I_{\text{ref}d-}}{m_2 - m_1} \\ A_3 &= m_1 \frac{I_{\text{ref}q+} - I_{\text{ref}q-}}{m_1 - m_2} \end{aligned}$$

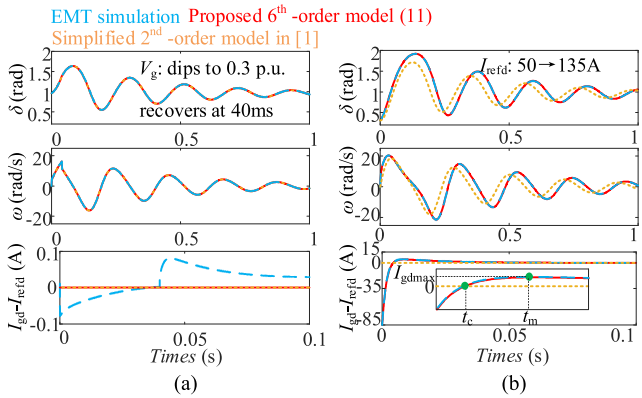

Fig. 3. Simulation verification of the proposed 6th-order model. (a) Under grid voltage dip disturbance. (b) Under current reference abrupt jump disturbance.

$$\begin{aligned} A_4 &= m_2 \frac{I_{\text{ref}q+} - I_{\text{ref}q-}}{m_2 - m_1} \\ m_1 &= \frac{-K_{\text{CP}}/L_f + \sqrt{(K_{\text{CP}}/L_f)^2 - 4K_{\text{CI}}/L_f}}{2} \\ m_2 &= \frac{-K_{\text{CP}}/L_f - \sqrt{(K_{\text{CP}}/L_f)^2 - 4K_{\text{CI}}/L_f}}{2}. \end{aligned} \tag{6}$$

Subscripts + and – denote the parameters after and before the disturbance, respectively. According to (5), dI_{gd}/dt is positive during 0-$t_{\max}$ and negative during $t_{\max}$-∞, under $I_{\text{ref}d}$ abrupt jumps. This means I_{gd} first rises from $I_{\text{ref}d-}$ monotonicity to the peak $I_{gd\max}$ at $t = t_{\max}$ and then monotonically drops to $I_{\text{ref}d+}$. The time that I_{gd} crosses $I_{\text{ref}d+}$ is defined as t_c. The expressions of the abovementioned values are derived as follows:

$$\begin{aligned} t_c &= \frac{\ln(-A_1/A_2)}{m_2 - m_1} \\ t_{\max} &= \frac{\ln(-m_1 A_1/m_2 A_2)}{m_2 - m_1} \\ I_{gd\max} &= I_{\text{ref}d+} + (I_{\text{ref}d+} - I_{\text{ref}d-})(m_1/m_2)^{\frac{1+m_1/m_2}{1-m_1/m_2}}. \end{aligned} \tag{7}$$

The simulation result in Fig. 3(b) is consistent with the monotonicity analysis above. It is mentioned that the above-mentioned decoupling characteristics only theoretically exist under stable conditions. The *dq*-axis currents and PLL dynamics cannot be completely decoupled due to control delay, converter modulation, and the digital filter in sampling circuit. However, under the ACC and PLL timescale studied in this article, these decoupling characteristics are reasonable under stable conditions.

B. Modeling of PLL

According to the control structure shown in Fig. 1(b), the dynamics of PLL can be obtained as

$$\begin{aligned} \mathrm{d}\theta_{\text{PLL}}/\mathrm{d}t &= \omega_{\text{PLL}} \\ \omega_{\text{PLL}} &= \omega_n + K_P V_{\text{PCC}q} + K_{\text{I}} \int V_{\text{PCC}q} \mathrm{d}t. \end{aligned} \tag{8}$$

Define the difference between PLL's output phase and grid phase as the virtual power angle of the system: $\delta = \theta_{\mathrm{PLL}}$-$\theta_{\mathrm{g}}$. Similarly, the virtual frequency is defined as the frequency difference between the PLL and the grid: $\omega = \omega_{\mathrm{PLL}}$-$\omega_g$. Take the time derivative of the second row of (8), we obtain

$$\mathrm{d}\omega/\mathrm{d}t = \mathrm{d}\omega_{\mathrm{PLL}}/\mathrm{d}t = K_P \mathrm{d}V_{\mathrm{PCC}q}/\mathrm{d}t + K_{\mathrm{I}} V_{\mathrm{PCC}q}. \quad (9)$$

According to the $V_{\mathrm{PCC}\,q}$ expression derived in (1), the expression of $\mathrm{d}V_{\mathrm{PCC}\,q}/\mathrm{d}t$ can be obtained as follows:

$$\begin{aligned}\mathrm{d}V_{\mathrm{PCC}q}/\mathrm{d}t &= -V_g\omega\cos\delta + \mathrm{d}\omega_{\mathrm{PLL}}/\mathrm{d}t L_g I_{gd} \\ &+ \omega_{\mathrm{PLL}} L_g \mathrm{d}I_{gd}/\mathrm{d}t + R_g \mathrm{d}I_{gq}/\mathrm{d}t + L_g \mathrm{d}^2 I_{gq}/\mathrm{d}t^2. \quad (10)\end{aligned}$$

Combining (1), (9), and (10), the state-space model of PLL considering nonideal ACC's coupling can be derived as

$$\begin{aligned}\mathrm{d}\delta/\mathrm{d}t &= \omega \\ \mathrm{d}\omega/\mathrm{d}t &= k_1 - k_2\sin\delta - (k_3 + k_4\cos\delta)\,\omega. \quad (11)\end{aligned}$$

The expressions of coefficients M and k_1–k_4 are denoted as

$$\begin{aligned}M &= (1 - K_P L_g I_{gd}) \\ k_1 &= \begin{pmatrix}\omega_n K_I L_g I_{gd} + K_I R_g I_{gq} + \omega_n K_P L_g \frac{\mathrm{d}I_{gd}}{\mathrm{d}t} \\ + K_P R_g \frac{\mathrm{d}I_{gq}}{\mathrm{d}t} + K_I L_g \frac{\mathrm{d}I_{gq}}{\mathrm{d}t} + K_P L_g \frac{\mathrm{d}^2 I_{gq}}{\mathrm{d}t^2}\end{pmatrix} \Big/ M \\ k_2 &= K_{\mathrm{I}} V_g / M \\ k_3 &= \left(-K_P L_g \frac{\mathrm{d}I_{gd}}{\mathrm{d}t} - K_I L_g I_{gd}\right) \Big/ M \\ k_4 &= K_P V_g / M. \quad (12)\end{aligned}$$

where k_1, $k_2\sin\delta$, and k_3+$k_4\cos\delta$ denote the equivalent mechanical torque, electromagnetic torque, and damping coefficient, respectively. Compared with the simplified PLL model ((1) and (2) in [5]) that neglects the ACC dynamic, there are mainly two differences: 1) terms related to I_{gd} and I_{gq}; 2) terms related to $\mathrm{d}I_{gd}/\mathrm{d}t$, $\mathrm{d}I_{gq}/\mathrm{d}t$ and $\mathrm{d}^2 I_{gq}/\mathrm{d}t^2$; Formula (5) and (11) together form the 6th-order model of GFLC that fully captures ACC dynamics.

With sufficient feed-forward terms in (3), the ACC can unilaterally decouple with the PLL and grid. This means ACC's dynamic is an autonomous subsystem, and will not be disturbed by the grid side disturbance and interaction. However, the PLL's dynamics will be affected by ACC's dynamics, according to (12). Consequently, disturbances such as grid voltage dips will not directly result in ACC transient processes, in which the simplified 2nd-order model (the yellow dotted curve) in [1] that assumes $I_{gdq} = I_{\mathrm{ref}\,dq}$ is still accurate compared to the EMT simulation (the blue dashed curve), as shown in Fig. 3(a). However, as shown in Fig. 3(b), the ACC transient dynamics is significant under current reference abrupt change disturbance, which usually happens in low voltage ride through process: $I_{\mathrm{ref}\,d}$ dips and $I_{\mathrm{ref}\,q}$ jumps at the fault occurrence moment; $I_{\mathrm{ref}\,d}$ jumps and $I_{\mathrm{ref}\,q}$ dips at the fault clearing moment. As shown in Fig. 3(b), under $I_{\mathrm{ref}\,d}$ jumps disturbance, the simplified 2nd-order model (the yellow dotted curve) shows non-negligible errors with the EMT simulation result (the blue dashed curve). In contrast, the proposed 6th-order model (the red solid curve) shows almost no errors compared with the EMT results (the blue dashed curve). The simplified 2nd-order model (the yellow dotted curve) shows less overshoot in power angle dynamics, which may yield over-optimistic misjudgment and it is unacceptable in engineering practice. Therefore, ACC's dynamics must be considered when estimating the transient stability boundary of GFLC under current reference abrupt change disturbances.

III. Transient Stability Assessment

In this section, the stability boundary of GFLC under current reference abrupt change disturbance is accurately estimated by the proposed iterative algorithm. First, an IFES concerning the mapping relation among output current, power angle, and PLL frequency under the critical stable condition is constructed based on the interaction mechanism between ACC and PLL. Then, an iterative algorithm is proposed to solve the above IFES. The critical stable boundary is thus obtained, with almost no conservatism. Furthermore, it is elaborated that the overall impact of nonideal ACC on GFLC's transient stability is always adverse, based on which a simplified but conservative stability evaluation method is proposed based on the inequality contraction. It is mentioned that as pointed out above, the *dq*-axis of ACC is decoupled, so only the *d*-axis disturbance is considered in this section due to the limited length. Taking the *q*-axis disturbance into account will not result in extra analysis difficulties.

A. Revelation of ACC and PLL Interaction Mechanism

To apply EAC or any other similar energy-based transient stability evaluation method, it is necessary to obtain the mapping relation between equivalent torques k_1–k_4 and power angle δ. As shown in formulas (11) and (12), the equivalent torques k_1–k_4 of GFLC are no longer constant and become time-variant due to the current dynamics: I_{gd} and $\dot{I}_{gd}$. However, only the time t distribution $I_{gd}(t)$ and $\dot{I}_{gd}(t)$ is explicit as shown in (5), while the power angle δ distribution $I_{gd}(\delta)$ and $\dot{I}_{gd}(\delta)$ remains unknown. The key to quantifying ACC's impacts on PLL is to bridge the gap of the explicit mapping relation between time t and power angle δ, which will be demonstrated below.

Considering that the ACC dynamics have already converged to the steady state when the PLL reaches the farthest point, the upper stability boundary can still be evaluated as the unstable equilibrium point δ_{uep}, which assumes $I_{gdq} = I_{\mathrm{ref}\,dq+}$

$$\delta_{\mathrm{uep}} = \pi - \sin^{-1}\left(\frac{\omega_n K_I L_g I_{\mathrm{ref}d+} + K_I R_g I_{\mathrm{ref}q+}}{K_P V_g}\right). \quad (13)$$

Integrating both sides of (11)'s second row, with δ_{uep} as the fixed upper limit and independent variable δ as the lower boundary can obtain the critically stable corresponding relation between frequency and power angle as shown in (14), in the form of integral with variable lower limit: x is the integration variable and δ is the function variable

$$\frac{\omega^2(\delta)}{2} = \int_{\delta}^{\delta_{\mathrm{uep}}} \begin{Bmatrix} k_1(x) - k_2(x)\sin x \\ -\left[k_3(x) + k_4(x)\cos x\right]\omega(x) \end{Bmatrix} \mathrm{d}x. \quad (14)$$

Formula (14) indicates that the EAC theory is equivalent to the energy conservation law, and both of their essentials are Newton's second law. In addition, another mapping relation

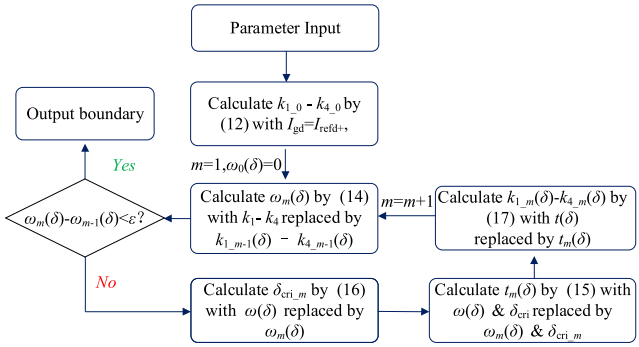

Fig. 4. Flowchart of the proposed iterative algorithm.

exists according to the physical definition of frequency

$$\frac{\mathrm{d}\delta}{\mathrm{d}t}=\omega\Rightarrow\frac{\mathrm{d}\delta}{\omega\left(\delta\right)}=\mathrm{d}t\Rightarrow t\left(\delta\right)=\int_{\delta_{\mathrm{cri}}}^{\delta}\frac{\mathrm{d}x}{\omega\left(x\right)}\tag{15}$$

where δ_{cri} is the critical lower boundary

$$\delta_{\mathrm{cri}}=\max\left\{\delta|\,\omega\left(\delta\right)=0\cap\delta<\delta_{\mathrm{uep}}\right\}\tag{16}$$

which can be solved by the iteration in Fig. 4. Formula (15) is in the form of integral with variable upper limit: x is the integration variable and δ is the function variable. Formula (15) indicates the critically stable corresponding relationship $t(\delta)$ between power angle δ and time t. Furthermore, the equivalent torques k_1–k_4 distribution concerning power angle δ can be obtained by combining (5), (12), and (15)

$$\begin{aligned}k_1\left(\delta\right)&=k_1\left\{I_{\mathrm{gd}}\left[t\left(\delta\right)\right]\quad\dot{I}_{\mathrm{gd}}\left[t\left(\delta\right)\right]\right\}\\k_2\left(\delta\right)&=k_2\left\{I_{\mathrm{gd}}\left[t\left(\delta\right)\right]\quad\dot{I}_{\mathrm{gd}}\left[t\left(\delta\right)\right]\right\}\\k_3\left(\delta\right)&=k_3\left\{I_{\mathrm{gd}}\left[t\left(\delta\right)\right]\quad\dot{I}_{\mathrm{gd}}\left[t\left(\delta\right)\right]\right\}\\k_4\left(\delta\right)&=k_4\left\{I_{\mathrm{gd}}\left[t\left(\delta\right)\right]\quad\dot{I}_{\mathrm{gd}}\left[t\left(\delta\right)\right]\right\}\end{aligned}\tag{17}$$

in which $k_{1\text{-}4}(I_{gd}, \mathrm{d}I_{gd}/\mathrm{d}t)$ are derived in (12), $I_{gd}(t)$ and $\mathrm{d}I_{gd}(t)/\mathrm{d}t$ are derived by (5), $t(\delta)$ is derived in (15). Equations (5) and (12)–(17) together form an IFES over the operation states I_{gd}, δ, and ω of GFLC, which is the mathematical essence of how the ACC and PLL interact with each other. This IFES is also the EAC equations set that fully captures ACC dynamics and damping effect, which denotes the states mapping relation $\omega(\delta)$ and $I_{gd}(\delta)$ under the critical stable condition, i.e., transient stability boundary.

B. Accurate Iterative Transient Stability Evaluation Method

The most intuitional method to solve IFES is the iterative algorithm. As shown in Fig. 4, an iterative algorithm is proposed to solve the above IFES. Pointed out that the subscript m denotes the iteration times. First, the initial values of torques k_{1_0}–k_{4_0} are calculated by assuming $I_{gd}=I_{\mathrm{refd+}}$, which ignores the ACC dynamics. In the mth times of iteration, the value of frequency distribution function $\omega_m(\delta)$ concerning power angle

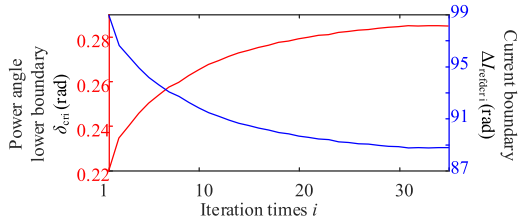

Fig. 5. Iteration results of power angle lower boundary δ_{cri} and current boundary $\Delta I_{\mathrm{refdcri}}$.

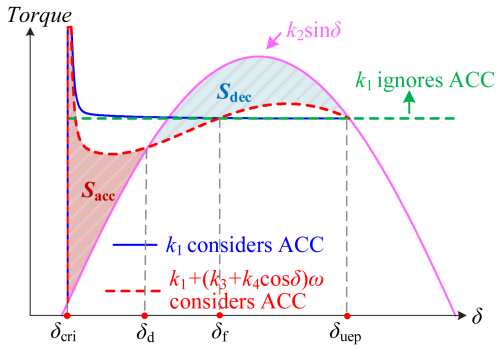

Fig. 6. EAC illustration of the proposed accurate iterative method.

δ is derived according to (14), based on the torque distribution function $k_{1\_m\text{-}1}(\delta)$-$k_{4\_m\text{-}1}(\delta)$ and the frequency distribution $\omega_{m\text{-}1}(\delta)$ from the m-1th iteration. Afterward, the critical lower boundary δ_{cri_m} of the mth iteration is derived according to (16), based on the above-mentioned frequency distribution function $\omega_m(\delta)$. Furthermore, the time distribution function $t_m(\delta)$ concerning power angle δ is calculated in (15), based on the above-mentioned frequency distribution function $\omega_m(\delta)$ and critical lower boundary δ_{cri_m}. Then, the torque distribution functions $k_{1\_m}(\delta)$-$k_{4\_m}(\delta)$ concerning δ are derived in (17), based on the above-mentioned time distribution function $t_m(\delta)$ concerning δ. The obtained torque distribution functions $k_{1\_m}(\delta)$-$k_{4\_m}(\delta)$ concerning δ will be utilized for the calculation of the frequency distribution function $\omega_{m+1}(\delta)$ in the m+1th times of iteration. The iteration stop condition is that the frequency distribution functions $\omega_m(\delta)$ concerning δ are converged within the given threshold value ε. The iteration results are displayed in Fig. 5, the proposed algorithm can quickly converge. The current boundary $\Delta I_{\mathrm{refdcri}}$ denotes the corresponding critical current disturbance degree. The converged frequency distribution function $\omega_{\mathrm{cri}}(\delta)$ and critical current distribution function $I_{\mathrm{gdcri}}(\delta)$ are thus the obtained transient stability boundary.

As shown in Fig. 6, the EAC illustration can be drawn based on the above-derived distribution functions $\omega_{\mathrm{cri}}(\delta)$ and $I_{\mathrm{gdcri}}(\delta)$, with whose help the torques distributions functions concerning power angle δ can be obtained: $k_1[I_{\mathrm{gdcri}}(\delta)]$, $k_2[I_{\mathrm{gdcri}}(\delta)]\sin\delta$, and $\omega_{\mathrm{cri}}(\delta)\{k_3[I_{\mathrm{gdcri}}(\delta)]+k_4[I_{\mathrm{gdcri}}(\delta)]\cos\delta\}$. The proposed accurate iterative method captures both the ACC dynamics and the damping effects, as the red dashed curve. The proposed method fully quantifies the torque variation $k_1(\delta)$–$k_4(\delta)$ attributed to the ACC's nonideal dynamics. Ignorance of either ACC dynamics or

damping effects will result in undesired stability misjudgment. The blue solid curve ignores damping effect and the green dashed line ignores both ACC and damping effect. The difference area between the blue solid curve and the green dashed line is the ACC's effects on k_1. It is seen that the extra accelerating area caused by the nonideal ACC (the part that green dashed line lower than blue solid curve) is significantly larger than the extra decelerating area (the part that green dashed line higher than blue solid curve), which means ACC's nonideal ACC dynamic always deteriorates GFLC's transient stability and it will be elaborated in detail in Section III-C. The difference area between the blue solid curve and the red dashed curve denotes the effect of nonlinear damping. It is seen that the damping can also yield both extra accelerating area (the part between zero damping point δ_f and $\delta_{\rm uep}$) and extra decelerating area (the part between $\delta_{\rm cri}$ and δ_f), playing an important role in GFLC's transient stability. Define the accelerating and decelerating areas that consider both ACC and damping effects as $S_{\rm acc}$ and $S_{\rm dec}$, respectively, shown as the red and blue areas in Fig. 6. The proposed method is based on the energy conservatism law in (14), so the EAC constraint is satisfied

$$\begin{aligned}
&S_{\rm acc}=\int_{\delta_{\rm cri}}^{\delta_{\rm d}}\\
&\begin{pmatrix}k_1\left(I_{\rm gdcri}\left(\delta\right)\right)-k_2\left(I_{\rm gdcri}\left(\delta\right)\right)\sin\delta\\-\left[k_3\left(I_{\rm gdcri}\left(\delta\right)\right)+k_4\left(I_{\rm gdcri}\left(\delta\right)\right)\cos\delta\right]\omega_{\rm cri}\left(\delta\right)\end{pmatrix}{\rm d}\delta\\
&S_{\rm acc}=-\int_{\delta_{\rm d}}^{\delta_{\rm uep}}\\
&\begin{pmatrix}k_1\left(I_{\rm gdcri}\left(\delta\right)\right)-k_2\left(I_{\rm gdcri}\left(\delta\right)\right)\sin\delta\\-\left[k_3\left(I_{\rm gdcri}\left(\delta\right)\right)+k_4\left(I_{\rm gdcri}\left(\delta\right)\right)\cos\delta\right]\omega_{\rm cri}\left(\delta\right)\end{pmatrix}{\rm d}\delta\\
&S_{\rm acc}=S_{\rm dec}
\end{aligned}\tag{18}$$

where δ_d is the power angle at which the acceleration is zero [i.e., the mechanical torque $k_1(\delta_{\rm d})$ equals the sum of the electromagnetic torque $k_2(\delta_d)\sin\delta_d$ and the damping torque $\omega(\delta_d)(k_3(\delta_d)+k_4(\delta_d)\cos\delta_d)$], as shown in Fig. 6.

C. Analysis of ACC's Adverse and Beneficial Effects

As pointed out by the EAC illustration in Fig. 6, the extra accelerating area (adverse effect) due to nonideal ACC is larger than the extra decelerating area (beneficial effect), which is elaborated in detail in Section III-C. First, it is proposed that ACC's effect can be approximated by the integral of current deviation with respect to power angle, denoted as $W_{a/b}$ in (19). Further derivation demonstrates that ACC's adverse effect $|W_b|$ on transient stability is always greater than the beneficial effect $|W_a|$. Below is the detailed elaboration.

Considering that $1>>I_{gd}K_PL_g$, the transient variation of $1/M$ can be approximately neglected. Therefore, the equivalent torques k_1 and k_3 can be assumed to be linear with the current I_{gd}, while k_2 and k_4 can be approximated as constant. Therefore, the nonideal ACC effects $W_{\rm extra}$ are proportional to the current deviation:

$$\begin{aligned}
W_{\rm extra}\approx&\int_{\delta_{\rm cri}}^{\delta_{\rm uep}}\left[k_1\left(I_{gd}\right)-\omega k_3\left(I_{gd}\right)\right]\\
&-\left[k_1\left(I_{{\rm ref}d+}\right)-\omega k_3\left(I_{{\rm ref}d+}\right)\right]{\rm d}\delta\\
&\propto\int_{\delta_{\rm cri}}^{\delta_{\rm uep}}I_{gd}-I_{{\rm ref}d+}{\rm d}\delta\\
=&\underbrace{\int_{\delta_{\rm cri}}^{\delta_c}I_{gd}-I_{{\rm ref}d+}{\rm d}\delta}_{-W_a}+\underbrace{\int_{\delta_c}^{\delta_{\rm uep}}I_{gd}-I_{{\rm ref}d+}{\rm d}\delta}_{-W_b}.
\end{aligned}\tag{19}$$

It is mentioned that the above approximation in facts yields a larger estimation $|W_a|$ in (19), so the correctness of the above conclusion $|W_b|>|W_a|$ is not affected. In addition, the ${\rm d}I_{gd}/{\rm d}t$ term is ignored because of its much faster dynamics and $K_P<<K_I$, to facilitate analysis. The ACC dynamic under current reference abrupt jump disturbance is shown in Fig. 3(b). During 0–t_c (defined as stage a), the current I_{gd} is lower than $I_{{\rm ref}d}$, and ignoring ACC dynamics will lead to lower mechanical torque k_1 and larger damping coefficient k_3, resulting in conservative stability evaluation results. During t_c-∞ (defined as stage b), the current I_{gd} is higher than $I_{{\rm ref}d}$, ignoring ACC dynamics will lead to larger mechanical torque k_1 and lower damping coefficient k_3, both resulting in over-optimistic stability results. Define the impulse of current deviation during stage a and stage b as C_a and C_b, respectively. As shown in (20), the overall current deviation impulse happens to be zero

$$\begin{aligned}
C_a=&\int_0^{t_c}I_{{\rm ref}d}-I_{gd}{\rm d}t=\int_0^{t_c}A_1e^{m_1t}+A_2e^{m_2t}{\rm d}t\\
C_b=&\int_{t_c}^{\infty}I_{{\rm ref}d}-I_{gd}{\rm d}t=\int_{t_c}^{\infty}A_1e^{m_1t}+A_2e^{m_2t}{\rm d}t\\
C_a+C_b=&\left.\frac{A_1}{m_1}e^{m_1t}+\frac{A_2}{m_2}e^{m_2t}\right|_0^{\infty}=0.
\end{aligned}\tag{20}$$

The frequency ω during stage a is obviously much smaller than that during stage b: $\omega(t_a)<<\omega(t_b)$. And t_c is relatively small compared to PLL's timescales. Therefore, the extra work due to the ACC dynamic is mainly attributed to stage b since $W_a<<W_b$:

$$\begin{aligned}
W_a=&\int_{\delta_{\rm cri}}^{\delta_c}I_{{\rm ref}d+}-I_{gd}{\rm d}\delta=\int_0^{t_c}\left(I_{{\rm ref}d+}-I_{gd}\right)\omega\left(t\right){\rm d}t\\
W_b=&\int_{\delta_c}^{\delta_{\rm uep}}I_{{\rm ref}d+}-I_{gd}{\rm d}\delta=\int_{t_c}^{\infty}\left(I_{{\rm ref}d+}-I_{gd}\right)\omega\left(t\right){\rm d}t\\
&W_a\ll-W_b
\end{aligned}\tag{21}$$

where δ_c is the power angle at $t=t_c$. This indicates the influence of ACC dynamics on transient stability is mainly reflected by the current overshoot during stage b. Consequently, the range of I_{gd} during transient processes can be approximated to be [$I_{{\rm ref}d+}$, $I_{gd\max}$], in the simplified but conservative method proposed in Section III-D to rapidly assess ACC's impact on stable boundaries.

D. Simplified Contractive Transient Stability Evaluation Method

To avoid unacceptable over-optimistic stability misjudgment, the worst conditions should be considered. That is, the mechanical torque k_1 should be contracted to its maximum possible value while the electromagnetic torque $k_2\sin\delta$ and damping coefficient $k_3+k_4\cos\delta$ should be contracted to its minimum possible value. The inequality contraction is conducted on the mechanical and electromagnetic torques and damping coefficients to derive a less-stable contracted 2nd-order system, whose stable boundary can be easily derived by our previous research [5], [21] and is taken as the conservative estimation of the original 6th-order system that considers nonideal ACC dynamics. Detailed mathematical inequality contraction is given below. First, derive the partial derivatives of k_1–k_4 concerning I_{gd}

$$\begin{aligned}
&\frac{\partial k_1}{\partial I_{gd}}\\
&=\begin{matrix}\omega_n K_I L_g\left(1-K_P L_g I_{gd}\right)\\ +K_P L_g\left(\omega_n K_I L_g I_{gd}+K_I R_g I_{gq}\right)\end{matrix}\Big/\left(1-K_P L_g I_{gd}\right)^2>0\\
&\frac{\partial k_2}{\partial I_{gd}}=\frac{K_I V_g K_P L_g}{\left(1-K_P L_g I_{gd}\right)^2}>0\\
&\frac{\partial k_3}{\partial I_{gd}}=\begin{matrix}-K_P L_g K_I L_g I_{gd}\\ -K_I L_g\left(1-K_P L_g I_{gd}\right)\end{matrix}\Big/\left(1-K_P L_g I_{gd}\right)^2<0\\
&\frac{\partial k_4}{\partial I_{gd}}=\frac{K_P^2 L_g V_g}{\left(1-K_P L_g I_{gd}\right)^2}>0.
\end{aligned}\tag{22}$$

Based on (22), k_1–k_4 can be contracted as in (23), which can be analytically derived from (12)

$$\begin{aligned}
&k_1\le\frac{\omega_n K_I L_g I_{gd\max}+K_I R_g I_{gq}}{1-K_P L_g I_{gd\max}}=k_{1\max}\\
&k_2\ge K_I V_g/\left(1-K_P L_g I_{\mathrm{refd}+}\right)=k_{2\min}\\
&k_3\ge\frac{-K_I L_g I_{gd\max}}{1-K_P L_g I_{gd\max}}=k_{3\min}\\
&k_{4\max}=K_P V_g/\left(1-K_P L_g I_{gd\max}\right)\ge k_4\\
&k_4\ge K_P V_g/\left(1-K_P L_g I_{\mathrm{refd}+}\right)=k_{4\min}.
\end{aligned}\tag{23}$$

With the contraction process in (23), the contracted 2nd-order system can be denoted as follows:

$$\begin{aligned}
\mathrm{d}^2\delta/\mathrm{d}t^2&=k_{1\max}-k_{2\min}\sin\delta\\
&\quad-\left(k_{3\min}+k_{4\min}\cos\delta\right)\omega,\delta<\pi/2\\
\mathrm{d}^2\delta/\mathrm{d}t^2&=k_{1\max}-k_{2\min}\sin\delta\\
&\quad-\left(k_{3\min}+k_{4\max}\cos\delta\right)\omega,\delta>\pi/2.
\end{aligned}\tag{24}$$

The contracted equivalent coefficients in the system (24) are no longer time-varying but constants, which are the same as the simplified model that ignores ACC dynamics [5]. Therefore, our previous EAC method [5] proposed under ideal ACC condition can be directly applied on (24) and is not repeated here. Due to the constant torque coefficients, the computational cost is much less than that of the accurate iterative method proposed in Section III-B, but with the scarifies of conservatism. However, the conservatism of the proposed inequality contraction method is relatively low and acceptable, as shown in Fig. 9. According to the $I_{gd\max}$ expression given in (7), it is linearly related to a function over $X=m_1/m_2$: $X^{(1+X)/(1-X)}$, which is usually less than 0.1. Considering the maintainer of transient stability, $I_{\mathrm{ref}d-}$ is usually not less than $0.3I_{\mathrm{ref}d+}$. Consequently, error due to partially assuming $I_{gd}\approx I_{gd\max}<1.07I_{\mathrm{ref}d+}$ in the proposed inequality contraction method is acceptable. Pointed out that the stability evaluation can be further simplified analytically if the path-dependence work of the nonlinear damping term is calculated based on the elliptic EAC method proposed in our earlier paper [21]. However, this increase in computing speed comes at the cost of increased conservatism.

IV. Discussion

The impact analyses of different ACC parameters on GFLC's transient stability are conducted in this section, which can provide guidance for GFLC parameter setting. In addition, a decoupled PLL control strategy is proposed to enhance transient stability by decoupling the ACC dynamics from the PLL dynamics. Moreover, a comparison is given between different transient stability analysis methods to demonstrate the superiority of the proposed method.

A. Parameters Impact Analyses

Since it is obvious that slower PLL bandwidth yields fewer interaction effects of ACC on PLL, this section only focuses on the effects of different ACC parameters. Under given PLL parameters, the interaction (W_{extra}) between PLL and ACC can be approximately analytically quantified by the current deviation impulse $|C_b|$

$$|C_{\mathrm{b}}|=A_1e^{m_1t_c}\frac{m_2-m_1}{m_1m_2}=\frac{I_{\mathrm{refd}+}-I_{\mathrm{refd}-}}{-m_2}\left(\frac{m_2}{m_1}\right)^{\frac{m_1}{(m_1-m_2)}}\tag{25}$$

which is affected by two negative real poles m_1 and m_2. Applying monotony analysis on (25) can conclude that the partial derivatives of $|C_b|$ concerning m_1 and m_2 are positive and negative, respectively

$$\begin{aligned}
&\partial|C_b|/\partial m_1>0\\
&\partial|C_b|/\partial m_2<0.
\end{aligned}\tag{26}$$

According to the expression of m_1 and m_2 in (6), the partial derivatives of m_1 and m_2 concerning ACC integral coefficient K_{CI} and proportional coefficient K_{CP} are derived as

$$\begin{aligned}
&\frac{\partial m_1}{\partial K_{\mathrm{CI}}}=\frac{1}{2L_f}\left(\frac{-4L_f}{\sqrt{{K_{\mathrm{CP}}}^2-4K_{\mathrm{CI}}L_f}}\right)<0\\
&\frac{\partial m_1}{\partial K_{\mathrm{CP}}}=\frac{1}{2L_f}\left(-1+\frac{K_{\mathrm{CP}}}{\sqrt{{K_{\mathrm{CP}}}^2-4K_{\mathrm{CI}}L_f}}\right)>0
\end{aligned}$$

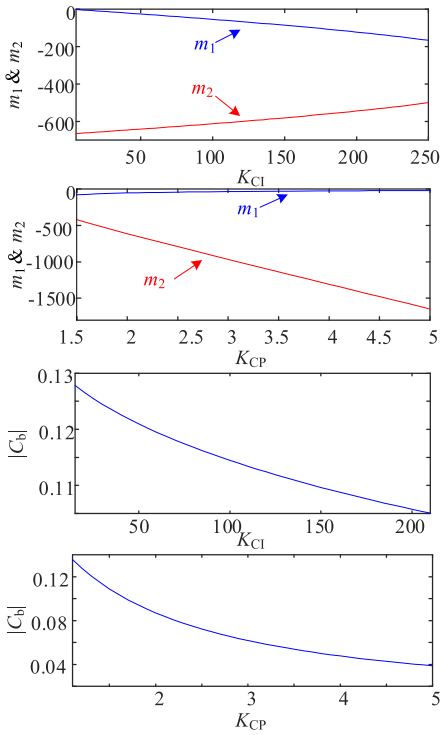

Fig. 7. Impacts of ACC integral coefficient K_{CI} and proportional coefficient K_{CP}.

$$\frac{\partial m_2}{\partial K_{CI}} = \frac{-1}{2L_f}\left(\frac{-4L_f}{\sqrt{{K_{CP}}^2 - 4K_{CI}L_f}}\right) > 0$$

$$\frac{\partial m_2}{\partial K_{CP}} = \frac{1}{2L_f}\left(-1 - \frac{K_{CP}}{\sqrt{{K_{CP}}^2 - 4K_{CI}L_f}}\right) < 0. \quad (27)$$

Therefore, partial derivatives of $|C_b|$ concerning K_{CI} and K_{CP} are both negative, based on the monotony transfusion of composite functions

$$\partial |C_b|/\partial K_{CP} < 0$$
$$\partial |C_b|/\partial K_{CI} < 0. \quad (28)$$

The abovementioned monotony analysis in (27), (28) is numerically verified in Fig. 7. Increasing both K_{CI} and K_{CP} will cause a less $|C_b|$, which indicates a more ideal ACC. In addition, formula (21) demonstrates that the total current deviation work is negative: the beneficial effect of the nonideal ACC during process *a* must be smaller than the adverse effect during process *b*. This yields that the dynamic of nonideal ACC is always adverse to GFLC's transient stability. Consequently, increasing K_{CI} and K_{CP} will both benefit transient stability since it can attenuate ACC's undesired transient process. However, too large K_{CI} may yield an underdamped ACC, which will result in unexpected oscillation. In practice, parameter-tuning process should comprehensively consider many factors including the dynamics performance. The discussion in this paper is only from the perspective of large-signal stability.

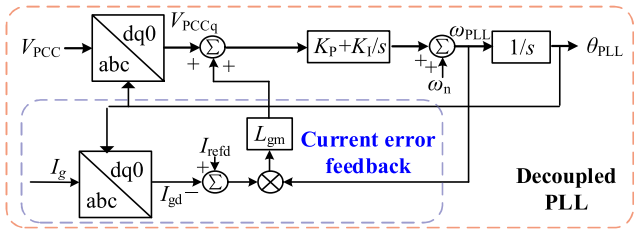

Fig. 8. Control structure of the proposed stability-enhanced decoupled PLL strategy.

B. Stability-Enhanced Decoupled PLL Control Strategy

As pointed out above, nonideal ACC dynamics always deteriorate the transient stability of GFLC. Therefore, a stability-enhanced decoupled PLL strategy is proposed in this section, which achieves the decoupling of PLL and ACC by adding a current error feedback term, so as to improve the transient stability. The proposed stability-enhanced decoupled PLL strategy structure is displayed in Fig. 8, which can be denoted as follows:

$$\theta_{PLL} = \int \left\{ \begin{matrix} \omega_n + K_P\left[V_{PCCq} + \omega_{PLL}L_g\left(I_{refd} - I_{gd}\right)\right] \\ +K_I\int\left[V_{PCCq} + \omega_{PLL}L_{gm}\left(I_{refd} - I_{gd}\right)\right]\mathrm{d}t \end{matrix} \right\} \mathrm{d}t \quad (29)$$

where L_{gm} is the online measurement value of grid inductance L_g [22]. Ignoring the measurement error, the state-space model of GFLC with this stability-enhanced decoupled PLL strategy can be derived by combining (1) and (29)

$$\begin{aligned} &\dot{\delta} = \omega \\ &\left(1 - K_P L_g I_{refd}\right)\dot{\omega} = K_I\omega_n L_g I_{refd} + K_I R_g I_{gq} \\ &- K_I V_g \sin\delta - \left(K_P V_g \cos\delta - K_I L_g I_{refd}\right)\omega \end{aligned} \quad (30)$$

which is the same as the simplified 2nd-order model that ignores ACC dynamics [1]. This yields that with the help of the current error feedback term added in the proposed stability-enhanced decoupled PLL strategy, the nonideal dynamics of ACC will no longer deteriorate the transient stability of GFLC. The ACC and PLL are completely decoupled with each other. Therefore, the parameter setting of ACC and PLL can be carried out independently, which greatly simplifies the controller parameter design process. It is mentioned that the proposed decoupled PLL strategy is not sensitive to L_g measurement errors: positive error (L_g<L_{gm}) yields better improvement in stability, while negative error (L_g>L_{gm}) will partially weaken the improvement but is always more stable than the conventional PLL. The robustness of the proposed decoupled PLL is simulationally and experimentally verified in Sections V and VI, respectively.

C. Comparison of Different Transient Stability Evaluation Methods

The comparison of different transient stability evaluation methods is given in Table I and Fig. 9. The parameters of the evaluated system are listed in Table II. The proposed accurate method is essentially a calculation-efficient substitute for the ODE method/ EMT simulation: almost conservatism-free but with less computation. This is because the proposed accurate

TABLE I
COMPARISON OF DIFFERENT TRANSIENT STABILITY EVALUATION METHODS

Method	Power angle boundary (rad)	Calculation
Accurate iterative method	[0.290, 2.182]	Slightly high
Simplified inequality contraction method	[0.374, 2.131]	Low
Time-domain try and trail	[0.289, 2.182]	Very high
Time-domain-based EAC [6]	[0.323, 2.182]	Very high
Bifurcation method [15]	[0.289, 2.182]	Very high
Lyapunov method [23] (ignore ACC and damping)	[0.752, 1.190]	\
Iterative EAC [5] (ignore ACC)	[0.221, 2.182]	\

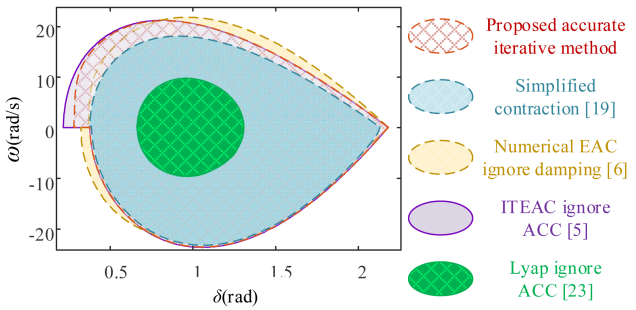

Fig. 9. Stable domain comparison of different stability evaluation methods.

TABLE II
PARAMETERS OF THE SIMULATION SYSTEM

Symbols	Description	Nominal value
V_{dc}	DC-link voltage of VSC	400 V
K_P, K_I	Controller parameters of PLL	0.1, 10
L_g	Grid inductance	3 mH
R_g	Gird resistance	0.03 Ω
L_f	Filter inductance	3 mH
K_{CP}, K_{CI}	Controller parameters of ACC	2, 100
V_g	Magnitude of microgrid voltage	$110\sqrt{2}$ V
ω_n	Rated angle frequency	100π rad/s
I_{refd}, I_{refq}	Magnitude of the reference current	135 A, 5 A
ε	Threshold of iteration	2×10^{-5} rad/s

method can be applied by matrix operations and can be further accelerated by pipeline algorithms. In addition, the proposed method can directly obtain the critical current disturbance value through one set of iteration, instead of iterating different disturbance values cyclically. The proposed iterative method fully captures the impacts of ACC dynamics and PLL's varying damping $k_3+k_4\cos\delta$ on GFLC's transient stability. Ignorance of ACC dynamics will lead to over-optimistic misjudgment, as the purple domain in Fig. 9, which is based on the ITEAC in [5]. Direct abandonment of the negative damping region leads to significant conservatism as the green domain in Fig. 9, which is derived by the conventional Lyapunov method [23]. The bifurcation theory-based method [15] is similar to the time domain discrete method. The EAC method in [6] seems like an analytic method apparently. However, it is still unclear how to obtain the critical disturbance. The critical interaction work is still quantified by time domain discrete integration in [6]. Therefore, the method in [6] is essentially still a time-domain try and trial. In addition, Wu et al. [6] do not even consider the adverse effect of PLL's varying damping on stability, the accuracy of [6] (the yellow domain in Fig. 9) is obviously much lower than that of the proposed accurate iterative method (the red domain in Fig. 9). The proposed simplified inequality contraction method (the blue domain in Fig. 9) demonstrates relatively high accuracy and much lower computation burden compared to the accurate iterative method, showing stronger practicability in online transient stability assessment. According to the evaluation results in Table I, the power angle boundary error of the simplified inequality contraction method compared to the accurate method is only 7.14%, which is acceptable in engineering practice but costs much less time for calculation. It is mentioned that $I_{gd} = I_{refd}$ is considered when deriving the $\omega<0$ part of the boundary in this article. This is because the ACC should have already reached the steady state long before the power angle reaches the farthest point and swings back.

V. SIMULATION VERIFICATION

In this section, MATLAB/Simulink-based simulations are conducted to verify the research results above, including

1) the high accuracy of the proposed iterative transient stability evaluation method that fully considers adverse impacts of nonideal ACC dynamics;
2) the ACC parameters impact trendy on transient stability;
3) better transient stability of the proposed decoupled PLL control strategy.

The parameters of the simulation system are listed in Table II.

A. Simulation Verification of the Proposed Transient Stability Evaluation Method

Considering that the stable domain estimated by the accurate iterative method completely includes the stable domain estimated by the simplified inequality contraction method, this section only verifies the former one's accuracy. With the parameters in Table II, the power angle lower boundary is calculated as $\delta_{cri} = 0.285$ rad, and the corresponding critical current reference disturbance is derived by regarding δ_{min} as the SEP of system (11): $\Delta I_{refdcri} = I_{refd}-(V_g\sin\delta_{min}-R_gI_{refq})/\omega_nL_g = 88.75$ A.

Simulation verification results are displayed in Fig. 10. Under the stable disturbance $\Delta I_{sta1} = 88$ A, the system can maintain stability and converge back to the SEP as shown in Fig. 10(a). However, the system will lose stability as shown in Fig. 10(b), when undergoing unstable disturbance $\Delta I_{uns1} = 89$ A that exceeds the derived stable boundary. It is seen that the trajectory of the critical disturbance almost overlaps the obtained stable boundary, showing the extremely high accuracy of the proposed stability evaluation method.

B. Verification of the ACC Parameters Impacts on Transient Stability

Simulation results with different ACC integral coefficients K_{CI} (= 50, 100, 400) are displayed in Fig. 11. With increasing K_{CI}, the dynamic response of ACC becomes faster and thus less

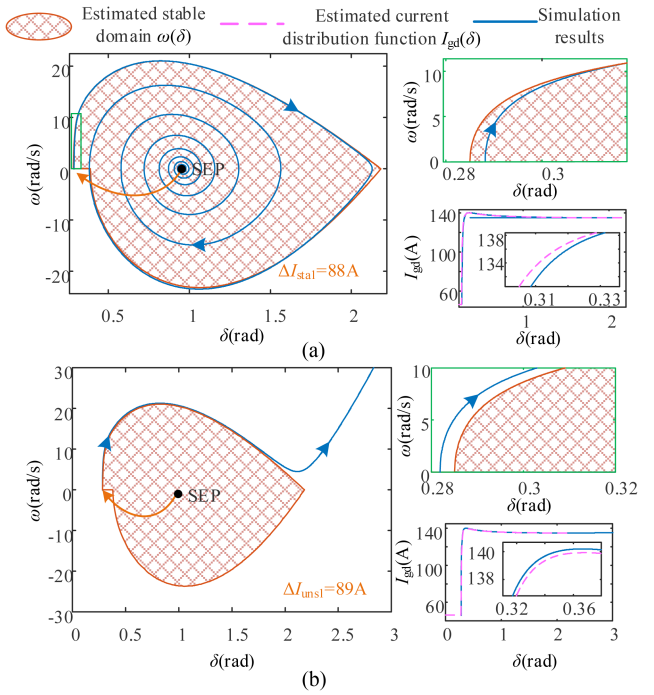

Fig. 10. Simulation verification of the proposed iterative transient stability evaluation method. (a) Stable case with $\Delta I_{\mathrm{sta1}} = 88$ A. (b) Unstable case with $\Delta I_{\mathrm{uns1}} = 89$ A.

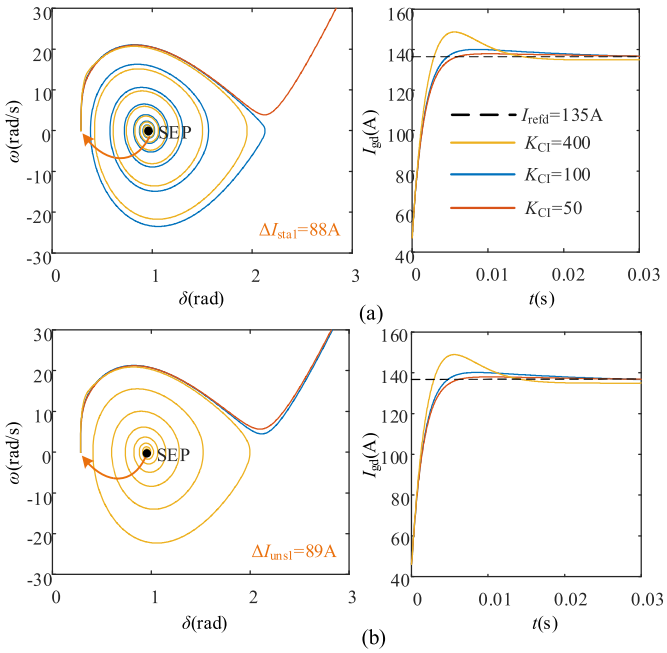

Fig. 11. Simulation verification of K_{CI}'s impact on transient stability. (a) Case 1 with $\Delta I_{\mathrm{sta1}} = 88$ A. (b) Case 2 with $\Delta I_{\mathrm{uns1}} = 89$ A.

adverse impacts on PLL's transient stability. Under $\Delta I_{\mathrm{sta1}} = 88$ A disturbance in Fig. 11(a), the system loses synchronization with $K_{\mathrm{CI}} = 50$, but can maintain stability with $K_{\mathrm{CI}} = 100$ and 400. Under $\Delta I_{\mathrm{uns1}} = 89$ A disturbance in Fig. 11(b), only the system with $K_{\mathrm{CI}} = 400$ can maintain stability. This means the stability is indeed enhanced by increasing ACC integral

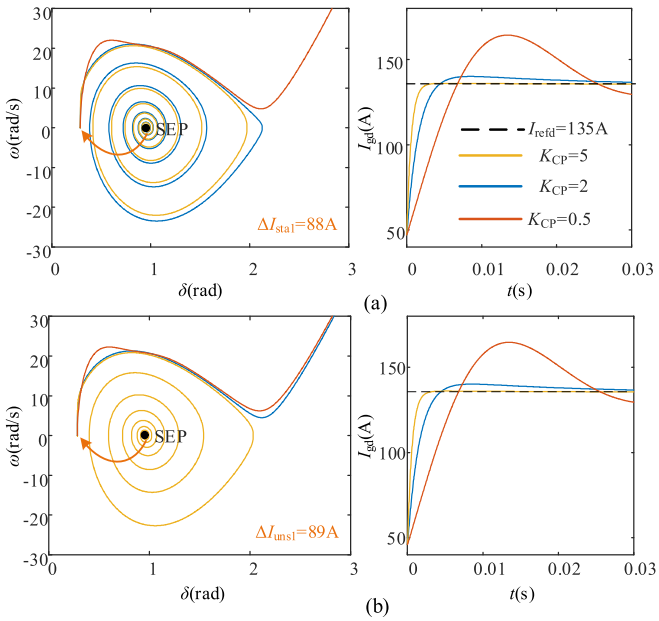

Fig. 12. Simulation verification of K_{CP}'s impact on transient stability. (a) Case 1 with $\Delta I_{\mathrm{sta1}} = 88$ A. (b) Case 2 with $\Delta I_{\mathrm{uns1}} = 89$ A.

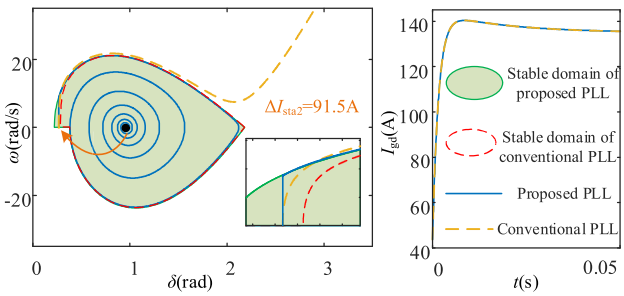

Fig. 13. Simulation verification of proposed stability-enhanced decoupled PLL under current disturbance $\Delta I_{\mathrm{sta2}} = 91.5$ A.

coefficient K_{CI}, which verifies the impact trend analysis in Section IV-B. However, K_{CI} cannot be selected too large to result in an underdamped ACC as the yellow curve in Fig. 11, which may deteriorate ACC dynamics. Similarly, simulation results with different ACC proportional coefficient K_{CP} (= 0.5, 2, 5) are displayed in Fig. 12. With the increase of K_{CP}, the dynamic response of ACC becomes faster and thus has less adverse impacts on GFLC's transient stability. Under $\Delta I_{\mathrm{sta1}} = 88$ A disturbance in Fig. 12(a), the system loses synchronization with $K_{\mathrm{CP}} = 0.5$ but can maintain stability with $K_{\mathrm{CP}} = 2$ and 5. Under $\Delta I_{\mathrm{uns1}} = 89$A disturbance in Fig. 12(b), only the system with $K_{\mathrm{CP}} = 5$ can maintain stability. This means the stability is indeed enhanced by increasing the ACC proportional coefficient K_{CP}, which verifies the impact trend analysis in Section IV-B.

C. Simulation Verification of the Proposed Stability-Enhanced Decoupled PLL Strategy

The stability enhancement of the proposed stability-enhanced decoupled PLL strategy is simulationally verified as shown in

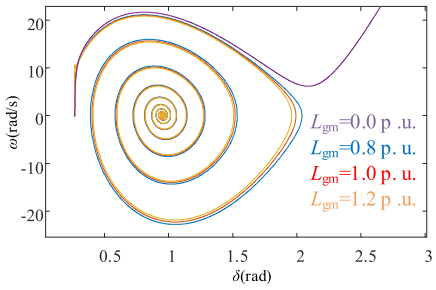

Fig. 14. Robustness verification of proposed stability-enhanced decoupled PLL under current disturbance $\Delta I_{\mathrm{sta3}} = 91$ A.

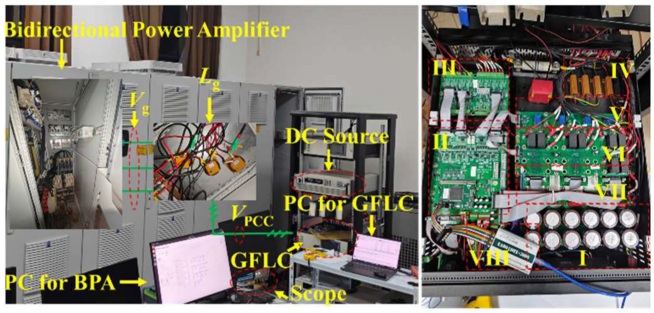

(a) (b)

Fig. 15. Prototype experiment platform: (a) overview and (b) zoom-in view of GFLC.

Fig. 13. With the help of the proposed stability-enhanced decoupled PLL strategy, the PLL dynamics are no longer affected by the nonideal ACC. Therefore, the iterative EAC [5] that ignores ACC dynamics can be directly applied in estimating its stable domain, as the green domain in Fig. 13. Due to the isolation of ACC's adverse impacts, the stable domain of the proposed stability-enhanced decoupled PLL fully includes the stable domain of the traditional PLL (the red dashed curve in Fig. 13). Under the current disturbance $\Delta I_{\mathrm{sta2}} = 91.5$ A, the tradition PLL loses stability as the yellow dashed curve in Fig. 13, since this disturbance already exceeds its boundary $\Delta I_{\mathrm{refdcri}} = 88.75$ A. However, this disturbance is still within the boundary (the green domain in Fig. 13) of the proposed stability-enhanced decoupled PLL strategy and the system can still maintain stability as the blue solid curve in Fig. 13. The transient stability enhancement of the proposed stability-enhanced decoupled PLL is thus verified.

Furthermore, the robustness of the proposed decoupled PLL strategy concerning L_g measurement error is verified by the simulation results in Fig. 14. It is seen that the system can still maintain stability with both negative error ($L_g = 0.8$ p.u.) and positive error ($L_{\mathrm{gm}} = 1.2$ p.u.), but will lose stability with the conventional PLL ($L_{\mathrm{gm}} = 0$). This demonstrates that the stability can still be enhanced with inaccurate L_g measurement, and the proposed decoupled PLL strategy is robust to weak grid inductance variation, which may occur in engineering practice.

VI. Prototype Experimental Verification

In this section, prototype experiments are conducted to verify the research results in this paper further. A 1.8-kW prototype experimental platform is established in Fig. 15, whose parameters are listed in Table III. The bidirectional power amplifier is controlled to produce three-phase symmetric ac power with constant voltage and frequency, to emulate the grid. The zoom-in view of the GFLC is given in Fig. 15(b), including I dc bus capacitance, II digital signal processor, III sampling board, IV precharge resistors, V current sensor, VI AC and DC relay, VII IGBT module, VIII compiler.

The prototype experiment results with different ACC parameters are displayed in Fig. 16. Under the same degree of current reference abrupt jump disturbance $\Delta I_{\mathrm{refd}} = 15.1$ A, the GFLC system with $K_{\mathrm{CP}} = 1.8$ and $K_{\mathrm{CI}} = 200$ can maintain

TABLE III
Parameters of the Prototype Experiment System

Symbols	Description	Nominal value
V_{dc}	DC-link voltage of VSC	260 V
K_{P}, K_{I}	Controller parameters of PLL	0.0417, 0.38
K_{CP}, K_{CI}	Controller parameters of ACC	1.8, 200
L_{g}	Grid inductance	4.5 mH
R_{g}	Gird resistance	2 Ω
V_{g}	Magnitude of microgrid voltage	60V
ω_{n}	Rated angle frequency	100π rad/s
L_{f}	Filter inductance	1 mH
I_{refd}, I_{refq}	Magnitude of the reference current	17.1A 0 A

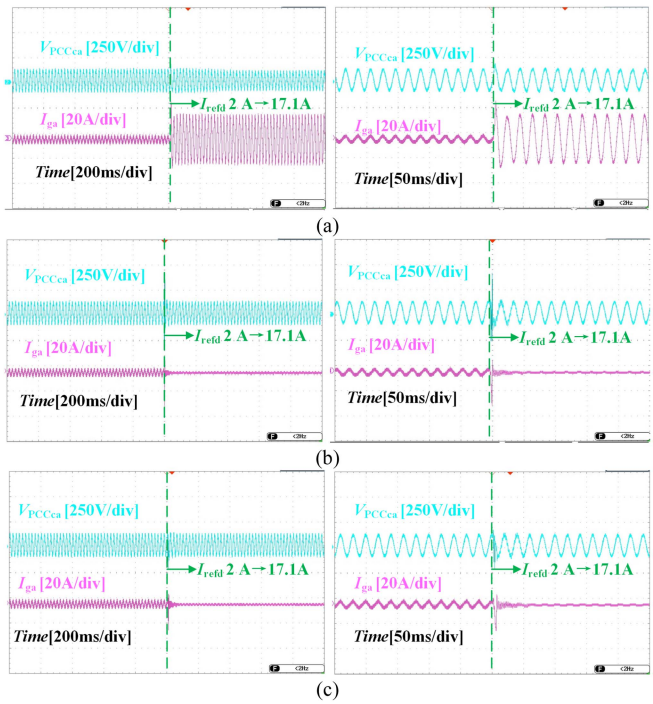

Fig. 16. Experimental results with different ACC parameters under current reference abrupt jump disturbance $\Delta I_{\mathrm{refd}} = 15.1$ A. (a) $K_{\mathrm{CP}} = 1.8$, $K_{\mathrm{CI}} = 200$, stable. (b) $K_{\mathrm{CP}} = 1.8$, $K_{\mathrm{CI}} = 170$, unstable. (a) $K_{\mathrm{CP}} = 1.5$, $K_{\mathrm{CI}} = 200$, unstable.

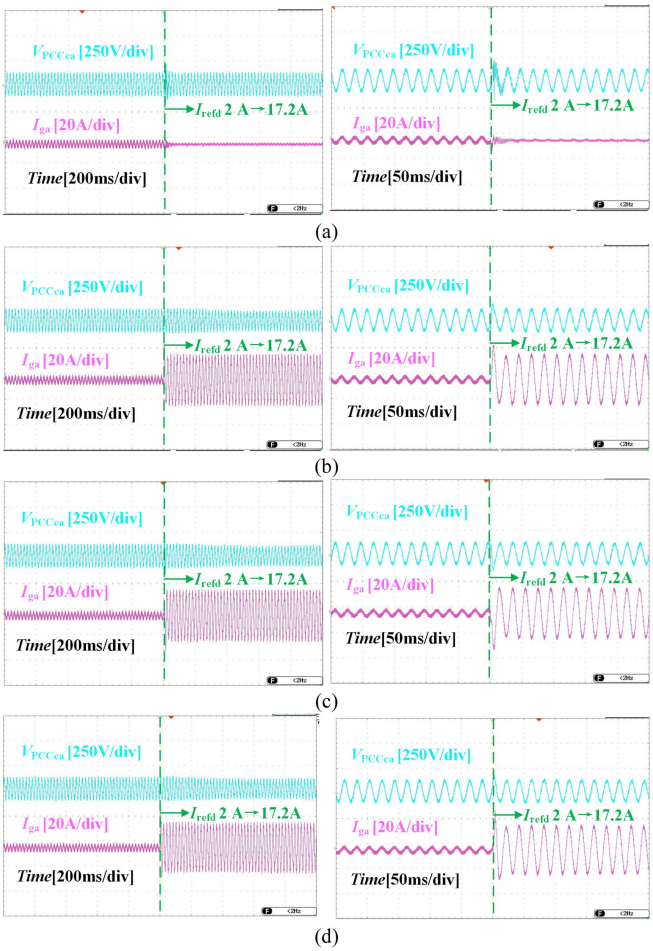

Fig. 17. Experimental verification of the proposed stability-enhanced decoupled PLL strategy under current reference abrupt jump disturbance $\Delta I_{\mathrm{ref}\,d} = 15.2$ A. (c) Conventional PLL, unstable. (b) Zero measurement error L_{gm}-$L_{\mathrm{g}} = 0$ mH, stable. (c) Positive measurement error L_{gm}-$L_{\mathrm{g}} = 1.5$ mH, stable. (d) Negative measurement error L_{gm}-$L_g = -1.5$ mH, stable.

stability as shown in Fig. 16(a), while the system with $K_{\mathrm{CP}} = 1.8$ and $K_{\mathrm{CI}} = 170$, and $K_{\mathrm{CP}} = 1.5$ and $K_{\mathrm{CI}} = 200$ both fail to synchronize with the grid, as shown in Fig. 16(b) and (c), respectively. This indicates that the transient stability of the GFLC is indeed enhanced with increased ACC proportional coefficient K_{CP} and integral coefficient K_{CI}. Consequently, the trendy impacts of ACC's parameters on transient stability are experimentally verified.

It is mentioned that the waveform after disturbance in Fig. 16(b) and (c) is attributed to the protection algorithm of the converter, which is triggered by the transient synchronous instability.

The prototype experimental verification of the proposed stability-enhanced decoupled PLL strategy stability enhancement is displayed in Fig. 17. Under the same current reference abrupt jump disturbance $\Delta I_{\mathrm{ref}\,d} = 15.2$ A, the conventional PLL fails to synchronous with the grid as shown in Fig. 17(a). In contrast, the proposed stability-enhanced decoupled PLL can maintain stability under the same disturbance as shown in Fig. 17(b). Therefore, the transient stability of GFLC is indeed enhanced with the help of the proposed stability-enhanced decoupled PLL strategy, compared to the conventional PLL. In addition, the system with either positive inductance measurement error ($L_{gm} = 6$ mH$>L_g = 4.5$ mH) or negative measurement error ($L_{gm} = 3$ mH$<L_g = 4.5$ mH) can both maintain stability as shown in Fig. 17(c) and (d), respectively, showing the robustness of the proposed stability-enhanced decoupled PLL strategy.

VII. Conclusion

This article analyzes the impacts of nonideal current alternating control on GFLCs' transient stability. The time domain response of ACC is analytically derived and an IFES over the operation states I_{gd}, δ, and ω of GFLC is constructed. By iterative calculation of the above IFES, the accurate estimation of the GFLC's transient stability boundary that fully captures ACC dynamics and damping effects is obtained. The accuracy of the proposed iterative transient stability evaluation method is almost the same as the time domain try and trial but with much less computation. In addition, a simplified transient stability assessment method based on inequality contraction is proposed, with further less computation and less but sufficient accuracy. Furthermore, the impact trends of ACC's proportional and integral coefficients are analytically revealed and a stability-enhanced decoupled PLL strategy is proposed by actively compensating current tracking error. Some conclusions are drawn as follows.

1) With appropriate feedforward terms, grid side disturbance or interaction between different converters will not yield much disturbance on ACC. The transient process of ACC is mainly due to the current reference abrupt change disturbance, which often occurs during fault ride-through processes.
2) The transient stable domain of GFLC that fully captures ACC's interaction is accurately derived based on the proposed method, with almost no conservatism.
3) The impacts of nonideal ACC are always adverse to GFLCs' transient stability, and the transient stability can be enhanced by increasing both the integral coefficient K_{CI} and proportional coefficient K_{CP} of ACC or actively compensating for current tracking errors in PLL.

In our future papers, the proposed method will be extended to analyze the inner voltage and current loops' impacts on grid-forming converters' transient stability.

References

[1] Y. Zhang, C. Zhang, and X. Cai, "Large-signal grid-synchronization stability analysis of PLL-based VSCs using Lyapunov's direct method," *IEEE Trans. Power Syst.*, vol. 37, no. 1, pp. 788–791, Jan. 2022.
[2] M. G. Taul, X. Wang, P. Davari, and F. Blaabjerg, "An overview of assessment methods for synchronization stability of grid-connected converters under severe symmetrical grid faults," *IEEE Trans. Power Electron.*, vol. 34, no. 10, pp. 9655–9670, Oct. 2019.
[3] C Zhang, M Molinas, Z Li, and X Cai, "Synchronizing stability analysis and region of attraction estimation of grid-feeding VSCs using sum-of-squares programming," *Front. Energy Res.*, vol. 8, 2020, Art. no. 56.
[4] Q. Hu, L. Fu, F. Ma, and F. Ji, "Large signal synchronizing instability of PLL-based VSC connected to weak AC grid," *IEEE Trans. Power Syst.*, vol. 34, no. 4, pp. 3220–3229, Jul. 2019.
[5] X. Li, Z. Tian, X. Zha, P. Sun, Y. Hu, and M. Huang, "An iterative equal area criterion for transient stability analysis of grid-tied converter systems with varying damping," *IEEE Trans. Power Syst.*, vol. 39, no. 1, pp. 1771–1784, Jan. 2024.

[6] C. Wu, Y. Lyu, Y. Wang, and F. Blaabjerg, "Transient synchronization stability analysis of grid-following converter considering the coupling effect of current loop and phase locked loop," *IEEE Trans. Energy Convers.*, vol. 39, no. 1, pp. 544–554, Mar. 2024.
[7] M. Zhao, X. Yuan, J. Hu, and Y. Yan, "Voltage dynamics of current control time-scale in a VSC-connected weak grid," *IEEE Trans. Power Syst.*, vol. 31, no. 4, pp. 2925–2937, Jul. 2016.
[8] P. Yu, Z. Tian, X. Zha, J. Sun, P. Zhong, and M. Huang, "Impact analysis of fast dynamics on stability of grid-tied inverter based on oscillator model and damping torque analysis," *IEEE Trans. Power Syst.*, vol. 37, no. 3, pp. 1881–1892, May 2022.
[9] U. Markovic, O. Stanojev, P. Aristidou, E. Vrettos, D. Callaway, and G. Hug, "Understanding small-signal stability of low-inertia systems," *IEEE Trans. Power Syst.*, vol. 36, no. 5, pp. 3997–4017, Sep. 2021.
[10] Y. Wang, X. Wang, F. Blaabjerg, and Z. Chen, "Harmonic instability assessment using State-space modeling and participation analysis in Inverter-Fed power systems," *IEEE Trans. Ind. Electron.*, vol. 64, no. 1, pp. 806–816, Jan. 2017.
[11] J. Chen, M. Liu, T. O'Donnell, and F. Milano, "Impact of current transients on the synchronization stability assessment of grid-feeding converters," *IEEE Trans. Power Syst.*, vol. 35, no. 5, pp. 4131–4134, Sep. 2020.
[12] Q. Hu, L. Fu, F. Ma, F. Ji, and Y. Zhang, "Analogized synchronous-generator model of PLL-based VSC and transient synchronizing stability of converter dominated power system," *IEEE Trans. Sustain. Energy*, vol. 12, no. 2, pp. 1174–1185, Apr. 2021.
[13] X. Fu, M. Huang, C. K. Tse, J. Yang, Y. Ling, and X. Zha, "Synchronization stability of grid-following VSC considering interactions of inner current loop and parallel-connected converters," *IEEE Trans. Smart Grid*, vol. 14, no. 6, pp. 4230–4241, Nov. 2023.
[14] Y. Ding, F. Gao, and M. M. Khan, "Transient stability analysis of microgrid considering impact of grid-following converter's current controller," *IEEE Trans. Power Electron.*, vol. 39, no. 8, pp. 9100–9105, Aug. 2024.
[15] C. C. Liu, J. Yang, C. K. Tse, and M. Huang, "Transient synchronization stability of grid-following converters considering non-ideal current loop," *IEEE Trans. Power Electron.*, vol. 38, no. 11, pp. 13757–13769, Nov. 2023.
[16] L. Huang, C. Wu, D. Zhou, F. Blaabjerg, and S. He, "Large-signal modeling of grid-following inverter: From sixth-order model to second-order model," in *Proc. IEEE 10th Int. Power Electron. Motion Control Conf.*, 2024, pp. 3413–3420.
[17] C. Wu, Z. Huang, Y. Wang, and F. Blaabjerg, "A new transient phenomenon caused by active current dynamics of grid-following converters during severe grid faults," *Front. Energy Res.*, vol. 12, Jul. 2024, Art. no. 1425105.
[18] Y. Ma, D. Zhu, Z. Zhang, X. Zou, J. Hu, and Y. Kang, "Modeling and transient stability analysis for type-3 wind turbines using singular perturbation and Lyapunov methods," *IEEE Trans. Ind. Electron.*, vol. 70, no. 8, pp. 8075–8086, Aug. 2023.
[19] X. Li, R. Zhang, Z. Tian, M. Huang, and X. Zha, "Quantitative impacts analysis of the inner current loop on grid-tied converters' Transient synchronous stability," in *Proc. IEEE 10th Int. Power Electron. Motion Control Conf.*, 2024, pp. 294–299.
[20] J. Xu, Z. Ling, Y. Luo, J. Kan, H. Diao, and S. Xie, "Synchronization stability analysis and parameter design of grid-following inverters considering the interactions of current control and phase-locked loop," *IEEE J. Emerg. Sel. Topics Power Electron.*, vol. 12, no. 5, pp. 5013–5027, Oct. 2024.
[21] X. Li et al., "A conservatism improved transient stability analysis of grid-following converters based on the proposed elliptic-equal area criterion," *IEEE Trans. Power Del.*, vol. 39, no. 2, pp. 1110–1123, Apr. 2024.
[22] M. Lu, W. Mu, M. Qin, A. Koehler, J. Fang, and S. M. Goetz, "Differential detection of feeder and mesh impedances through a series–Parallel direct-injection soft open point," *IEEE Trans. Power Electron.*, vol. 40, no. 1, pp. 1964–1973, Jan. 2025.
[23] X. Fu et al., "Large-signal stability of grid-forming and grid-following controls in voltage source converter: A comparative study," *IEEE Trans. Power Electron.*, vol. 36, no. 7, pp. 7832–7840, Jul. 2021.

Xilin Li was born in Wuhan, Hubei Province, China, in 1999. He received the B.Eng. degree major in electrical engineering and minor in computer science, in 2021, from Wuhan University, Wuhan, China, where he is currently working toward the Ph.D. degree in electrical engineering.

His research interests include the control and transient stability analysis of converter-based power systems.

Pan Feng was born in Xingtai, Hebei Province, China, in 2002. He received the B.Eng. degree in electrical engineering from Sichuan University, Chengdu, China, in 2023. He is currently working toward the Ph.D. degree in electrical engineering with Wuhan University, Wuhan, China.

His research interests include the modeling and stability analysis of virtual synchronous generator-based and dc-link voltage-synchronized-based grid-forming converters.

Ruiqi Zhang was born in Tianjin, China, in 2002. He is currently working toward the B.Eng. degree in electrical engineering with Wuhan University, Wuhan, China, where he will be working toward the Ph.D. degree in electrical engineering since September 2025.

His research interests include stability analysis in grid-connected converters and applications of complex network in power system.

Zhen Tian (Member, IEEE) received the B.S. degree in electrical engineering from Wuhan University, Wuhan, China, in 2014, and the Ph.D. degree in control science and engineering from Shanghai Jiao Tong University, Shanghai, China, in 2019.

During 2017–2019, he was a visiting Scholar with the Department of Electrical and Computer Engineering, Illinois Institute of Technology, Chicago, USA. He has been with the School of Electrical Engineering and Automation, Wuhan University, since 2019, where he is currently an Associate Professor. His research interests mainly include modeling, control and stability analysis of renewable energy generation, microgrid, and power-electronics-enabled power systems.

Meng Huang (Member, IEEE) received the B.Eng. and M.Eng. degrees in electronic science and technology from the Huazhong University of Science and Technology, Wuhan, China, in 2006 and 2008, respectively, and the Ph.D. degree in electrical engineering from the Hong Kong Polytechnic University, Hong Kong, China, in 2013.

He is currently a Professor with the School of Electrical Engineering and Automation, Wuhan University, Wuhan, China. His research interests include the safe operation and control of grid-connected systems.

Dr. Huang was the recipient of the Best Paper Award of IEEE TRANSACTIONS ON POWER ELECTRONICS in 2016. He serves as an Editor of International Journal of Circuit Theory and Applications, and has served as the Guest Editor for IEEE JOURNAL OF EMERGING AND SELECTED TOPICS OF CIRCUITS AND SYSTEMS, the Guest Associate Editor of IEEE TRANSACTIONS ON INDUSTRIAL APPLICATIONS and IEEE JOURNAL OF EMERGING AND SELECTED TOPICS OF POWER ELECTRONICS.

Xiaoming Zha (Senior Member, IEEE) was born in Huaining, Anhui Province, China, in 1967. He received the B.S., M.S., and Ph.D. degrees in electrical engineering from Wuhan University, Wuhan, China, in 1989, 1992, and 2001, respectively.

He was a Postdoctoral Fellow with the University of Alberta, Edmonton, AB, Canada, from 2001 to 2003. He has been a Faculty Member of Wuhan University since 1992, and became a Professor, in 2003. He is currently the Deputy Dean with the School of Electrical Engineering, Wuhan University. His research interests include power electronic converter, the application of power electronics in smart grid and renewable energy generation, the analysis and control of microgrid, the analysis and control of power quality, and frequency control of high-voltage high-power electric motors.

Xiaoling Xiong (Member, IEEE) received the B.S., M.S., and Ph.D. degrees in electrical engineering from the Nanjing University of Aeronautics and Astronautics, Nanjing, China, in 2007, 2010, and 2015, respectively.

From 2011 to 2012, she was a Research Assistant with the Department of Electronic and Information Engineering, Hong Kong Polytechnic University, Hong Kong, China. Since 2015, she has been with North China Electric Power University, Beijing, China, where she is currently an Associate Professor. Simultaneously, she was with Aalborg University, Aalborg, Denmark, where she was a Visiting Postdoctoral with the Department of Energy Technology from 2018 to 2020. Her current research interests include HVdc system, modeling, analysis, and design power electronic systems and study the nonlinear behaviors in power electronic circuits.

Pan Hu (Senior Member, IEEE) was born in Wuhan, Hubei Province, P.R. China, on August 18, 1989. He received the B.E. degree in electrical engineering from Wuhan Textile University, Wuhan, China, in 2012, and the Ph.D. degree in electrical engineering from the School of Electrical Engineering and Automation, Wuhan University, Wuhan, China, in 2018.

In 2017, he was a Visiting Ph.D. Student with Energy System Department, University of Alberta, Edmonton, AB, Canada. Since 2018, he has been a Senior Engineer and Research Staff with the State Grid Hubei Electric Power Research Institute, China. He has authored more than 30 articles, and more than four inventions. His research interests include renewable energy planning, power system stability analysis and control, and power quality mitigation.